

Magnetospheric accretion and spin-down of the prototypical classical T Tauri star AA Tau

J.-F. Donati^{1*}, M.B. Skelly¹, J. Bouvier², S.G. Gregory³, K.N. Grankin⁴, M.M. Jardine⁵, G.A.J. Hussain⁶, F. M enard², C. Dougados², Y. Unruh⁷, S. Mohanty⁷, M. Auri ere¹, J. Morin^{8,1}, R. Far es¹ & the MaPP collaboration

¹ *LATT-UMR 5572, CNRS & Univ. de Toulouse, 14 Av. E. Belin, F-31400 Toulouse, France*

² *LAOG-UMR 5571, CNRS & Univ. J. Fourier, 414 rue de la Piscine, F-38041 Grenoble, France*

³ *School of Physics, Univ. of Exeter, Stocker Road, Exeter EX4 4QL, UK*

⁴ *Crimean Astrophysical Observatory, Nauchny, Crimea 334413, Ukraine*

⁵ *School of Physics and Astronomy, Univ. of St Andrews, St Andrews, Scotland KY16 9SS, UK*

⁶ *ESO, Karl-Schwarzschild-Str. 2, D-85748 Garching, Germany*

⁷ *Department of Physics, Imperial College London, London SW7 2AZ, UK*

⁸ *Dublin Institute for Advanced Studies, School of Cosmic Physics, 31 Fitzwilliam Place, Dublin 2, Ireland*

2010 June, MNRAS, submitted

ABSTRACT

From observations collected with the ESPaDOnS spectropolarimeter at the Canada-France-Hawaii Telescope (CFHT) and with the NARVAL spectropolarimeter at the T elescope Bernard Lyot (TBL), we report the detection of Zeeman signatures on the prototypical classical T Tauri star (cTTS) AA Tau, both in photospheric lines and accretion-powered emission lines. Using time series of unpolarized and circularly polarized spectra, we reconstruct at two epochs maps of the magnetic field, surface brightness and accretion-powered emission of AA Tau. We find that AA Tau hosts a 2 – 3 kG magnetic dipole tilted at $\simeq 20^\circ$ to the rotation axis, and of presumably dynamo origin. We also show that the magnetic poles of AA Tau host large cool spots at photospheric level and accretion regions at chromospheric level.

The accretion rate at the surface AA Tau at the time of our observations (estimated from the emission in the He I D_3 line mainly) is strongly variable, ranging from -9.6 to -8.5 and equal to -9.2 in average (in logarithmic scale and in $M_\odot \text{ yr}^{-1}$); this is an order of magnitude smaller than the disc accretion rate at which the magnetic truncation radius (below which the disc is disrupted by the stellar magnetic field) matches the corotation radius (where the Keplerian period equals the stellar rotation period) – a necessary condition for accretion to occur. It suggests that AA Tau is largely in the propeller regime, with most of the accreting material in the inner disc regions being expelled outwards and only a small fraction accreted towards the surface of the star. The strong variability in the observed surface mass-accretion rate and the systematic time-lag of optical occultations (by the warped accretion disc) with respect to magnetic and accretion-powered emission maxima also support this conclusion.

Our results imply that AA Tau is being actively spun-down by the star-disc magnetic coupling and appears as an ideal laboratory for studying angular momentum losses of forming Suns in the propeller regime.

Key words: stars: magnetic fields – stars: formation – stars: imaging – stars: rotation – stars: individual: AA Tau – techniques: spectropolarimetry

1 INTRODUCTION

Classical T Tauri stars (cTTSs) are young low-mass stars still contracting towards the main sequence and surrounded by gaseous and dusty accretion discs; they represent the im-

* E-mail: donati@ast.obs-mip.fr

portant formation stage that stars with masses lower than $\simeq 3 M_{\odot}$ undergo at an age of a few Myrs, and during which they build up their exotic planetary systems.

Observations reveal that magnetic fields play a crucial role at the cTTS stage. Thanks to strong large-scale fields (e.g., Donati & Landstreet 2009, for a review), cTTSs are able to evacuate the core regions of their accretion discs, and to connect to the inner rim of their discs via discrete accretion funnels or veils through which material is accreted and angular momentum is dissipated (e.g., Bouvier et al. 2007a, for a review). Accretion discs are also expected to be magnetic, with fields enhancing accretion rates, generating powerful jets and modifying planet formation/migration mechanisms. Surveys of the magnetic properties of cTTSs and their accretion discs are thus critically needed to understand the early history of low-mass stars in general and of the Sun in particular.

Magnetic Protostars and Planets (MaPP) is an international project focussing specifically on this issue. It has been granted 690 hr of observing time over 9 consecutive semesters (2008b to 2012b) with the ESPaDOnS spectropolarimeter on the 3.8-m Canada-France-Hawaii Telescope (CFHT) to survey 15 cTTSs and 3 protostellar accretion discs of FU Ori type (FUOrs); it also regularly benefits from contemporaneous observations with the NARVAL spectropolarimeter on the 2-m Télescope Bernard Lyot (TBL) as well as photometric observations from Crimea, Uzbekistan and Armenia. Additional multiwavelength observations from space (e.g., XMM-Newton/Chandra/HST) and/or from the ground (e.g., HARPS) are also organised in conjunction with MaPP campaigns on a few specific targets, providing deeper insights into the physical processes under scrutiny (and in particular magnetospheric accretion).

MaPP primarily collects spectropolarimetric data probing the large-scale magnetic fields of cTTSs through the Zeeman signatures they generate in photospheric line profiles; it also allows the detection of Zeeman signatures in the accretion spots located at the footpoints of accretion funnels. By monitoring these Zeeman signatures over several successive rotation cycles (to filter out intrinsic variability and to retrieve rotational modulation more reliably and efficiently), MaPP can reconstruct maps of the large-scale magnetic fields of cTTSs and simultaneously recover the location of accretion spots. By extrapolating from surface magnetograms, one can finally obtain an approximate 3D description of the magnetosphere, allowing more realistic and quantitative models of the geometry of accretion funnels and more generally of the star/disc magnetic coupling. Initial pre-MaPP studies of a few cTTSs were presented in several publications (Donati et al. 2007, 2008a; Jardine et al. 2008; Gregory et al. 2008; Hussain et al. 2009; Donati et al. 2010) to validate the main assumptions underlying the imaging code and demonstrate the overall feasibility of the modelling.

The present paper is the first in a series dedicated to MaPP data and results, using a more general and better suited set of modelling assumptions and a more mature version of the imaging code; ultimately, the main goal is to provide estimates and statistics on the topologies of large-scale magnetic fields of cTTSs and on the locations of their accretion spots, allowing the diagnosis of how they correlate with, e.g., stellar masses and rotation rates (in a way similar to

that achieved on main-sequence stars, Donati & Landstreet 2009), but also on parameters more specific to cTTSs, e.g., ages and accretion/ejection properties. This first MaPP study concentrates on the prototypical cTTS AA Tau (see Sec. 2 for a quick summary of the main stellar parameters relevant to this study). We report here spectropolarimetric and photometric observations of AA Tau (Sec. 3), describe the variations of photospheric lines and accretion proxies (Sec. 4) and their subsequent modelling (Sec. 5). We finally discuss the implications of these new results for our understanding of magnetospheric accretion processes in cTTSs (Sec. 6).

2 AA TAU

AA Tau is a well-known cTTS showing strong H α emission and IR excesses demonstrating the presence of a gaseous and dusty accretion disc surrounding the protostar (e.g., Bouvier et al. 1999). A fit to the observed BVRI photometric fluxes (showing $B - V$, $V - R_c$ and $V - I_c$ colors of 1.5, 0.9 and 1.9 respectively at times of maximum brightness and minimum accretion, see Figs. 3 and 6 of Bouvier et al. 2003) suggests that AA Tau has a photospheric temperature of $T_{\text{eff}} \simeq 4000$ K and a visual reddening of $A_V \simeq 0.8$ mag (Bouvier et al. 1999), implying a visual bolometric correction of -1.8 (Bessell et al. 1998). Given its distance ($\simeq 140$ pc) and maximum visual brightness (corresponding to a magnitude of $\simeq 12.3$, e.g., Grankin et al. 2007), AA Tau has a bolometric luminosity equal to that of the Sun (within about 0.1 dex) and thus a radius of $R_{\star} \simeq 2 R_{\odot}$, suggesting a mass of $M_{\star} \simeq 0.7 M_{\odot}$ and an age of about 1.5 Myr (Siess et al. 2000) in agreement with previous estimates (e.g., Bouvier et al. 1999). This implies in particular that AA Tau is fully convective and very similar (in mass, radius, age and rotation rate) to the other prototypical cTTS BP Tau (Donati et al. 2008a).

AA Tau is known to undergo periodic eclipses with irregular depths, likely caused by partial occultations by a warped accretion disc viewed close to edge-on (Bouvier et al. 1999, 2003, 2007b). As the warp in the accretion disc is presumably caused by the magnetic field of the star, the recurrence period of these eclipses, equal to 8.22 ± 0.03 d (Bouvier et al. 2007b), is actually tracing the rotation period of the star. Given that $R_{\star} \simeq 2 R_{\odot}$, the estimated rotation period implies that the equatorial rotation velocity of AA Tau is 12.3 km s^{-1} ; the measured line-of-sight projected rotation velocity (denoted $v \sin i$ where i is the inclination of the rotation axis to the line of sight, and equal to $11.3 \pm 0.7 \text{ km s}^{-1}$ Bouvier et al. 2003) independently confirms that AA Tau is viewed from the Earth at an inclination angle of about $70 \pm 10^\circ$. With these parameters, the radius at which the Keplerian period is equal to the rotation period of the star, called the corotation radius and denoted r_{cor} , is equal to $\simeq 7.6 R_{\star}$ or 0.07 AU.

Mass accretion on AA Tau is reported to be smaller than the average rate expected for cTTSs of similar masses (e.g., Johns-Krull 2007). The spectrum of AA Tau exhibits all the usual accretion proxies, in particular H α , H β , He I D_3 and Ca II infrared triplet (IRT) emission. From their strength (in particular that of He I emission) and the corresponding line fluxes (see Sec. 3) in our spectra, and using

empirical correlations from the published literature (e.g., Fang et al. 2009), we can estimate the logarithmic mass-accretion rate at the surface of AA Tau (in $M_{\odot} \text{ yr}^{-1}$), found to vary from -9.6 to -8.5 throughout our runs (e.g., in 2008 December) and equal to about -9.2 in average. This is up to 10 times smaller than the accretion rate of BP Tau (equal to -8.6 when estimated with the same method, Donati et al. 2010). Accretion on AA Tau is known to be intrinsically variable on a time scale of a few days (e.g., Bouvier et al. 2003, 2007b). Optical veiling, i.e., the apparent weakening of the photospheric spectrum (presumably caused by accretion), is also often observed at a moderate (and variable) level on AA Tau (e.g., Bouvier et al. 2003, 2007b).

3 OBSERVATIONS

Spectropolarimetric observations of AA Tau were collected in 2008 December and 2009 January using ESPaDOnS on the CFHT. ESPaDOnS collects stellar spectra spanning the whole optical domain (from 370 to 1,000 nm) at a resolving power of 65,000 (i.e., 4.6 km s^{-1}) and with a spectral sampling of 2.6 km s^{-1} , in either circular or linear polarisation (Donati 2003). A total of 18 circular polarisation spectra were collected in 2 separate blocks shifted by about 1 month, with 11 spectra over a period of 15 d in 2008 December and 7 spectra over a period of 8 d in 2009 January; all polarisation spectra consist of 4 individual subexposures lasting each 1200 s and taken in different polarimeter configurations to allow the removal of all spurious polarisation signatures at first order. Six additional spectra were collected a year before (in 2007 December and 2008 January) over a period of 12 d, with the ESPaDOnS twin NARVAL on the TBL, with slightly shorter exposure times.

All raw frames are processed with LIBRE ESPRIT, a fully automatic reduction package/pipeline available at CFHT and TBL. It automatically performs optimal extraction of ESPaDOnS unpolarized (Stokes I) and circularly polarized (Stokes V) spectra grossly following the procedure described in Donati et al. (1997). The velocity step corresponding to CCD pixels is about 2.6 km s^{-1} ; however, thanks to the fact that the spectrograph slit is tilted with respect to the CCD lines, spectra corresponding to different CCD columns across each order feature a different pixel sampling. LIBRE ESPRIT uses this opportunity to carry out optimal extraction of each spectrum on a sampling grid denser than the original CCD sampling, with a spectral velocity step set to about 0.7 CCD pixel (i.e. 1.8 km s^{-1}). All spectra are automatically corrected of spectral shifts resulting from instrumental effects (e.g., mechanical flexures, temperature or pressure variations) using telluric lines as a reference. Though not perfect, this procedure provides spectra with a relative radial velocity (RV) precision of better than 0.030 km s^{-1} (e.g., Donati et al. 2008b).

The peak signal-to-noise ratios (S/N, per 2.6 km s^{-1} velocity bin) achieved on the collected spectra (i.e., the sequence of 4 subexposures) range between 100 and 200 for ESPaDOnS data (except for one spectrum recorded in poor weather conditions) and between 60 and 90 for NARVAL data (directly reflecting the smaller collecting area). Rotational cycles E are computed from heliocentric Julian dates

Table 1. Journal of ESPaDOnS/CFHT observations collected in 2008 December and 2009 January. Columns 1–4 respectively list the UT date, the heliocentric Julian date and UT time (both at mid-exposure), and the peak signal to noise ratio (per 2.6 km s^{-1} velocity bin) of each observation (i.e., each sequence of $4 \times 1200 \text{ s}$ subexposures). Column 5 lists the rms noise level (relative to the unpolarized continuum level I_c and per 1.8 km s^{-1} velocity bin) in the circular polarization profile produced by Least-Squares Deconvolution (LSD), while column 6 indicates the rotational cycle associated with each exposure (using the ephemeris given by Eq. 1).

Date	HJD (2,454,000+)	UT (h:m:s)	S/N	σ_{LSD} ($10^{-4}I_c$)	Cycle (1+)
Dec 06	806.97106	11:11:06	180	2.5	48.510
Dec 07	807.92124	09:59:24	200	2.3	48.625
Dec 08	808.94040	10:27:02	160	3.0	48.749
Dec 09	809.94201	10:29:24	130	3.7	48.871
Dec 10	810.92881	10:10:27	100	5.8	48.991
Dec 15	815.92556	10:06:02	190	2.4	49.599
Dec 16	816.90946	09:42:55	60	8.7	49.719
Dec 17	817.90170	09:31:49	140	3.7	49.840
Dec 18	818.89873	09:27:36	160	3.2	49.961
Dec 19	819.89824	09:26:57	110	4.6	50.082
Dec 20	820.89756	09:26:02	120	4.3	50.204
Jan 07	838.78706	06:48:28	160	2.8	52.380
Jan 09	840.75479	06:02:13	180	2.6	52.620
Jan 10	841.74685	05:50:53	190	2.3	52.740
Jan 11	842.89978	09:31:14	140	3.8	52.881
Jan 12	843.79311	06:57:43	110	4.9	52.989
Jan 13	844.73006	05:27:02	130	3.9	53.103
Jan 14	845.75784	06:07:09	180	2.7	53.228

Table 2. Same as Table 1 for the additional NARVAL/TBL observations collected in 2007 December and 2008 January. The exposure time of each sequence slightly varies (from 4×1000 to $4 \times 1200 \text{ s}$) from night to night.

Date	HJD (2,454,000+)	UT (h:m:s)	S/N	σ_{LSD} ($10^{-4}I_c$)	Cycle (1+)
Dec 27	462.36191	20:35:13	70	10.0	6.587
Dec 31	465.54716	01:02:15	80	7.0	6.974
Dec 31	466.37216	20:50:19	90	6.1	7.075
Jan 01	467.37235	20:50:41	80	7.7	7.196
Jan 03	468.55236	01:10:01	60	8.3	7.340
Jan 07	473.38037	21:02:49	70	7.2	7.927

according to the ephemeris:

$$\text{HJD} = 2454400.0 + 8.22E \quad (1)$$

where the rotation period is taken from Bouvier et al. (2007b). The full journal of observations is presented in Tables 1 & 2 for ESPaDOnS/CFHT and NARVAL/TBL data respectively.

Least-Squares Deconvolution (LSD, Donati et al. 1997) was applied to all observations. The line list we employed for LSD is computed from an ATLAS9 LTE model atmosphere (Kurucz 1993) and corresponds to a K7 spectral type ($T_{\text{eff}} = 4,000 \text{ K}$ and $\log g = 3.5$) appropriate for AA Tau. Only moderate to strong atomic spectral lines (with line-to-continuum core depressions larger than 40% prior to all

non-thermal broadening) are included in this list; spectral regions with strong lines mostly formed outside the photosphere (e.g., Balmer, He, Ca II H, K and IRT lines) and/or heavily crowded with telluric lines were discarded. Altogether, more than 9,000 spectral features are used in this process, with about 40% of them from Fe I. Expressed in units of the unpolarized continuum level I_c , the average noise levels of the resulting Stokes V LSD signatures are ranging from 2.3 to 5.7×10^{-4} per 1.8 km s^{-1} velocity bin for ESPaDOnS data (except on Dec 16) and from 6 to 10×10^{-4} for NARVAL data.

For estimating when eclipses of AA Tau are occurring, contemporaneous photometry was collected from Crimean Astrophysical Observatory (CrAO) over a period extending about 1 month before and after the main spectropolarimetric runs; a total of 5 and 13 measurements were obtained in conjunction with our 2008/2009 and 2007/2008 runs respectively. Additional photometric data from the All-Sky Automated Survey (ASAS, Pojmanski 1997) were added to improve phase coverage; selecting only grade A exposures, and further rejecting statistically deviant points, we are left with 12 and 9 supplementary ASAS measurements contemporaneous with our 2008/2009 and 2007/2008 runs. Typical rms photometric accuracies are about 50 and 100 mmag for CrAO and ASAS data respectively.

4 VARIATIONS OF PHOTOSPHERIC LINES AND ACCRETION PROXIES

Zeeman signatures with typical peak-to-peak amplitudes of about 1% are clearly detected at all times in LSD profiles of photospheric lines (see Fig. 1 top right panel); temporal variations are also detected but remain moderate, the average Stokes V profile over the whole run featuring a roughly symmetric shape (with respect to line centre) suggesting the presence of a significant toroidal field component at the surface of the star (e.g., Donati et al. 2005). As a result, the line-of-sight projected component of the field averaged over the visible stellar hemisphere (called longitudinal field and estimated from the first moment of the Stokes V profile, Donati et al. 1997) is weak, varying from -230 G to $+70 \text{ G}$ during the 2008/2009 observing run depending on the epoch (see Fig. 2 lower left panel).

LSD Stokes I profiles of photospheric lines also vary with time, both in position and strength (see Fig. 1 top left panel). The corresponding RV variations reach a peak-to-peak amplitude of about 2 km s^{-1} (about a mean of about 17 km s^{-1}), similar to previous results reporting that these variations are apparently stable on a long-term basis and tentatively attributed to spots at the surface of AA Tau (Bouvier et al. 2007b). By comparing our spectra of AA Tau to those of a spectroscopic template of similar spectral type, we can in principle retrieve estimates of the veiling, i.e., the amount by which photospheric lines are weakened with respect to those of the template star. The template star we observed (61 Cyg B, of similar temperature but different luminosity class) shows LSD profiles that are weaker (by 10 – 30%) than most of our AA Tau profiles. While it first indicates that a better template star is needed to obtain absolute veiling estimates, it at least suggests that veiling is only moderate for AA Tau at the time of our observations.

Using our strongest LSD profile of AA Tau (at cycle 53.103) as a zero-veiling reference, we find that veiling is most of the time smaller than 5% during the 2008/2009 observing run, except between rotation cycles 49.7 – 50.2 where it peaks at about 20% (see Fig. 2 lower right panel).

We find that LSD Stokes I and V profiles collected at similar rotation phases can exhibit different shapes at different rotation cycles (e.g., at cycles 48.991, 49.961 and 52.989), indicating that intrinsic variability is significant. In particular, veiling does not repeat well between successive rotation cycles (see Fig. 2 lower right panel), suggesting that this intrinsic variability likely reflects unsteady accretion at the surface of AA Tau. We note that veiling remains smaller than 5% throughout our 2009 January observations (rotation cycle 52.3 – 53.3), suggesting that we are catching AA Tau in a state of constantly very low accretion at this time of the 2008/2009 run; we suspect that, as a result, this is also an epoch at which rotational modulation of spectral lines is easiest to detect against intrinsic variability. We finally note that strong veiling (when present) occurs at rotation phases 0.8 – 1.1 in the 2008/2009 run, i.e., slightly before eclipse maximum (at phase 1.05, see Fig. 2 upper panel) and similar to previous reports (e.g., Bouvier et al. 2007b).

Usually considered as the most reliable accretion proxy, He I D_3 emission at 587.562 nm is thought to be produced in the postshock region at the footpoints of accretion funnels, i.e., in chromospheric accretion spots. At the time of our observations, He I emission always shows up as a narrow profile (see Fig. 3, top panel) and amounts to an average equivalent width of about 15 km s^{-1} (i.e., 0.030 nm). It is strongly variable with time, with equivalent widths varying from 7.5 to 45 km s^{-1} (i.e., 0.015 to 0.090 nm) throughout our 2008/2009 run (see Fig. 2 second panel right column). Previous studies (e.g., Bouvier et al. 2003, 2007b) report very similar levels of He I emission, equal to about 25 km s^{-1} in average (i.e., 0.05 nm), most of the time lower than 50 km s^{-1} (i.e., 0.10 nm) and reaching at most 75 km s^{-1} (i.e., 0.15 nm) during highest-accretion episodes. Times of strongest He I emission clearly coincide with epochs of maximum veiling, as previously reported in the literature (e.g., Bouvier et al. 2007b); in particular, using the published correlation between veiling and He I emission (see Fig. 5 of Bouvier et al. 2007b), we can safely confirm that veiling is indeed very small at rotational cycle 53.103 (assumed as our zero-veiling reference epoch, see above). Most of the observed variation of He I emission does not repeat from one rotation cycle to the next and thus mostly reflects intrinsic variability rather than rotational modulation. We find that He I emission is minimal throughout our 2009 January observations, with equivalent widths varying from 7.5 to 10.2 km s^{-1} (i.e., 0.015–0.020 nm); it confirms that rotation cycle 52.3 – 53.3 corresponds to a very-low-accretion stage of AA Tau with limited (i.e., $\simeq 30\%$ peak-to-peak) though definite rotational modulation, and with maximum emission occurring around phase 1.0.

Clear Zeeman signatures are detected in conjunction with He I D_3 emission, corresponding to longitudinal fields as strong as -2.5 kG (see Fig. 2 second panel left column) and similar to previous published reports (e.g., Valenti & Johns-Krull 2004). We note that longitudinal fields are not markedly different in phases of low and high

accretion, indirectly confirming that He I emission is mostly probing accretion spots at the footpoints of accretion funnels; as a result, intrinsic variability on this longitudinal field estimate is limited while rotational modulation is fairly clear. Longitudinal field is strongest around phase 1.0 (i.e., in phase with line emission), indicating that this is when the accretion spot is best visible to an Earth-based observer.

Core emission in Ca II IRT lines are also useful for probing magnetospheric accretion. Since Ca II emission is presumably also coming from the non-accreting chromosphere, it is less specifically related to accretion spots than He I emission and is thus a more ambiguous proxy. However, the redder spectral location, higher magnetic sensitivity and multiple nature of the corresponding spectral lines more than compensate for this drawback; moreover, the shape of the corresponding Zeeman signatures is simpler (i.e., featuring a classical, nearly-antisymmetric pattern, as opposed to the strongly non-antisymmetric Zeeman signatures of the He I line, e.g., Donati et al. 2007, 2008a) and thus easier to model. To extract the core Ca II emission profiles (used later in the imaging analysis, see Sec. 5) from our spectra, we start by constructing a LSD-like weighted average of the 3 IRT lines; we then subtract the underlying (much wider) photospheric absorption profile, with a Lorentzian fit to the far wings over a velocity interval of $\pm 200 \text{ km s}^{-1}$ about the emission core. Equivalent widths of the Ca II emission are in average equal to about 15 km s^{-1} (i.e., 0.043 nm) and vary from 12 to 24 km s^{-1} (i.e., $0.035 - 0.070 \text{ nm}$) during our 2008/2009 run. As for He I, most of the variation does not repeat between successive rotation cycles (see Fig. 1 bottom left panel and Fig. 2 third panel right column) and is thus intrinsic in nature. Note however that the strongest Ca II emission episode (at cycle 48.510) coincides with no more than a small increase in He I emission (see Fig. 2 right column) while large He I emission episodes generate only moderate Ca II emission; this directly relates to the fact that Ca II emission is more sensitive to chromospheric activity and flares (the likely cause of the emission episode at cycle 48.510) than He I emission. During rotation cycle 52.3–53.3 (i.e., in 2009 January), Ca II emission is close to minimum, varying by about 20% peak to peak; maximum emission is reached at about phase 1.0 (as for He I emission, see Fig. 2 middle panels right column), confirming that most of the observed rotational modulation at this time of the run is due to the chromospheric accretion spot.

Zeeman signatures in Ca II IRT lines are clearly detected at almost all epochs, with average peak-to-peak amplitudes of about 10% (see Fig. 1 bottom right panel). Corresponding longitudinal fields reach up to about -1 kG in high accretion states (-0.9 and -1.2 kG at cycles 49.961 and 50.082 respectively) and more typically range from 0 to -700 G otherwise. In 2009 January in particular (rotation cycles 52.3 – 53.3), longitudinal fields vary very smoothly, and in phase with longitudinal fields derived from the He I line; this is further evidence that the observed fluctuation mainly reflects rotational modulation. Maximum field is reached at phase 0.95, i.e., when the accretion spot faces the observer; maximum field strength is about 3 times weaker than that from He I lines, suggesting that the accretion spot contributes no more than about one fourth to Ca II emission (the remaining part coming from the non-accreting chromosphere).

H α and H β both feature emission components of varying strengths (see Fig. 3 bottom panel); while H α emission is strong and wide and truncated by a central absorption component (giving the profile a mostly double-peak appearance), H β emission is much weaker and mostly confined to the blue profile wing. During the 2008/2009 run, the average equivalent width of H α is 550 km s^{-1} (1.2 nm), with peaks of up to 2050 km s^{-1} (4.5 nm , at cycle 48.991). For H β , the average equivalent width is close to 0 (within about 20 km s^{-1} or 0.03 nm), with the weak blue-wing emission barely compensating for the central absorption; at cycle 48.991, H β emission peaks at an equivalent width of 430 km s^{-1} (0.7 nm).

In 2009 January, H α is weakest, with an average equivalent width of 250 km s^{-1} (0.55 nm); blue and red emission components vary more or less in phase with each other, peaking around phase 0.35 and minimum at phase 0.85. At the same time, H β exhibits strong central absorption and reduced blue-wing emission, with an average equivalent width as low as -70 km s^{-1} (-0.1 nm) and profile variation concentrating mainly in the red wing (at about $+100 \text{ km s}^{-1}$); maximum and minimum emission occur at phase 0.5 and 1.0 respectively. Following Bouvier et al. (2007b), we speculate that the absorption episodes in the red wing emission of H β trace accretion funnels crossing the line of sight as they corotate around the star.

Using the average equivalents widths of the He I line, the Ca II IRT and H α during our 2008/2009 run, we derive logarithmic line fluxes (with respect to the luminosity of the Sun L_{\odot}) equal to -5.3 , -5.1 and -3.6 respectively. This implies a logarithmic accretion luminosity (with respect to L_{\odot}) of -2.3 ± 0.3 using the empirical correlations of Fang et al. (2009) and putting strong weight on the He I data, and thus a logarithmic mass-accretion rate at the surface of the star of -9.2 ± 0.3 (in $M_{\odot} \text{ yr}^{-1}$). Mass accretion rates can also be estimated (though more roughly) through the full width of H α at 10% height (e.g., Natta et al. 2004; Cieza et al. 2010); in our case, the full widths we determine range from 350 km s^{-1} (in 2009 January) up to 480 km s^{-1} (at cycle 48.991), with an average of about 420 km s^{-1} , yielding logarithmic mass-accretion rates of -9.5 , -8.8 and -8.2 (with typical errors of ± 0.6) respectively supporting our main estimates. We find that the logarithmic surface mass-accretion rate at magnetic maximum (i.e., around phase 0.0) can vary by about an order of magnitude (from -9.4 to -8.5) from one cycle to the next, while that at magnetic minimum (i.e., around phase 0.5) is more stable on the long term (at about -9.6). During the low-accretion phase of 2009 January, the logarithmic mass-accretion rate at the surface of AA Tau is found to be -9.5 in average and to vary by only $\simeq 50\%$ peak-to-peak (from -9.6 to -9.4).

For our 2007/2008 run, we obtain similar results (not shown here) but with larger error bars and worse phase sampling (7 phases only, the first 6 roughly covering one cycle, see Table 2). Zeeman signatures in Stokes V LSD profiles of photospheric lines are again detected at all phases, tracing longitudinal fields of $+90$ to -220 G . Emission in Ca II and He I lines vary smoothly with time, reaching maximum strengths at phase 1.3; longitudinal fields from the Ca II lines also show smooth changes from 0 to -730 G , reaching maximum field at phase 1.2. This suggests in particular that the accretion spot is located at phase 1.2-1.3, i.e.,

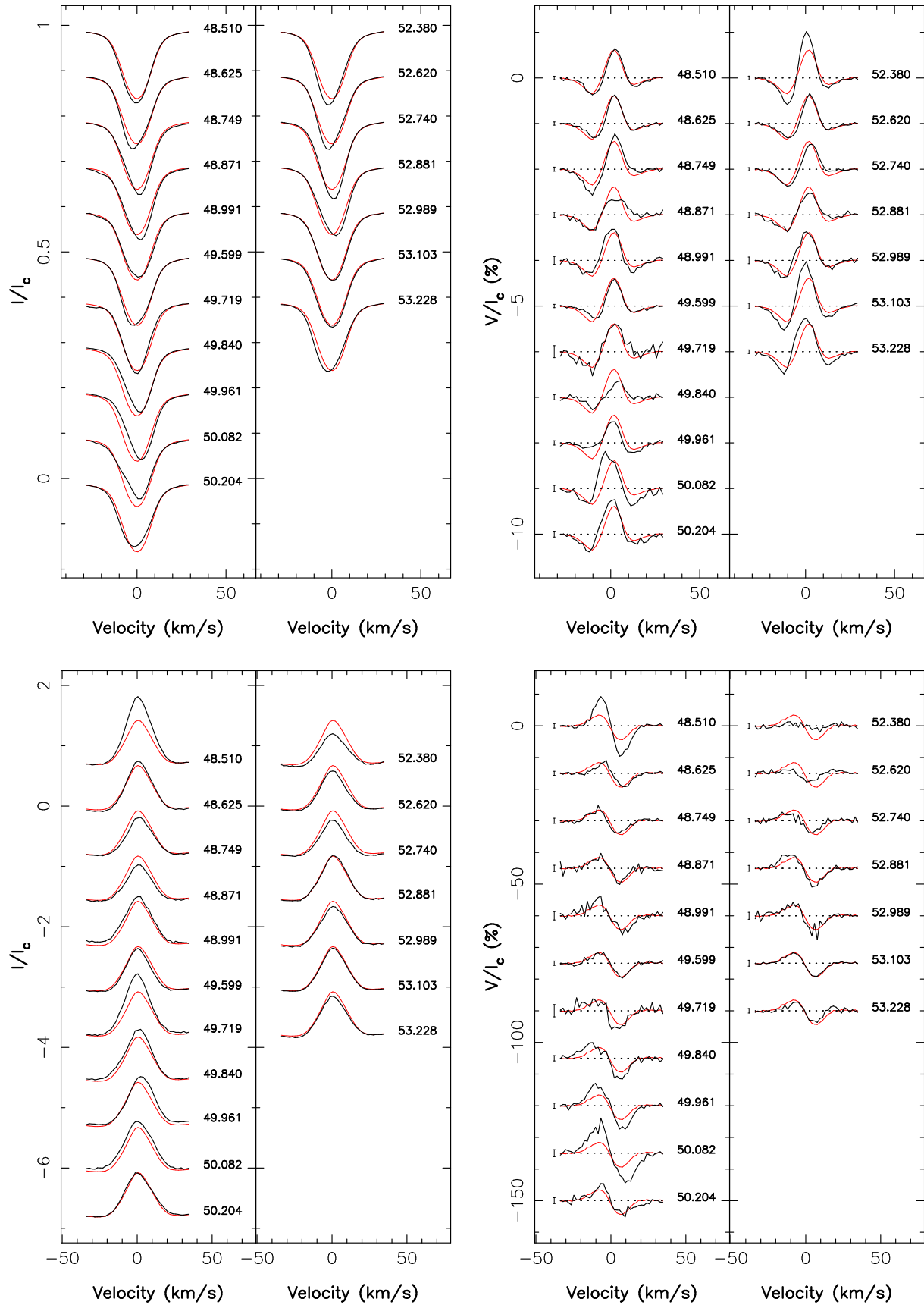


Figure 1. Temporal variations of the Stokes *I* (left) and Stokes *V* (right) LSD profiles of the photospheric lines (top) and of the Ca II emission (averaged over the 3 IRT lines, bottom) of AA Tau in 2008 December (left column of each panel) and 2009 January (right column). The Stokes *I* profiles of Ca II emission is shown before subtracting the underlying (much wider) photospheric absorption, hence the reduced flux in the far wings (with respect to the unit continuum). To emphasize variability, the average profile over the run is shown in red. Rotation cycles (as listed in Table 1) and 3σ error bars (for Stokes *V* data only) are also included next to each profile.

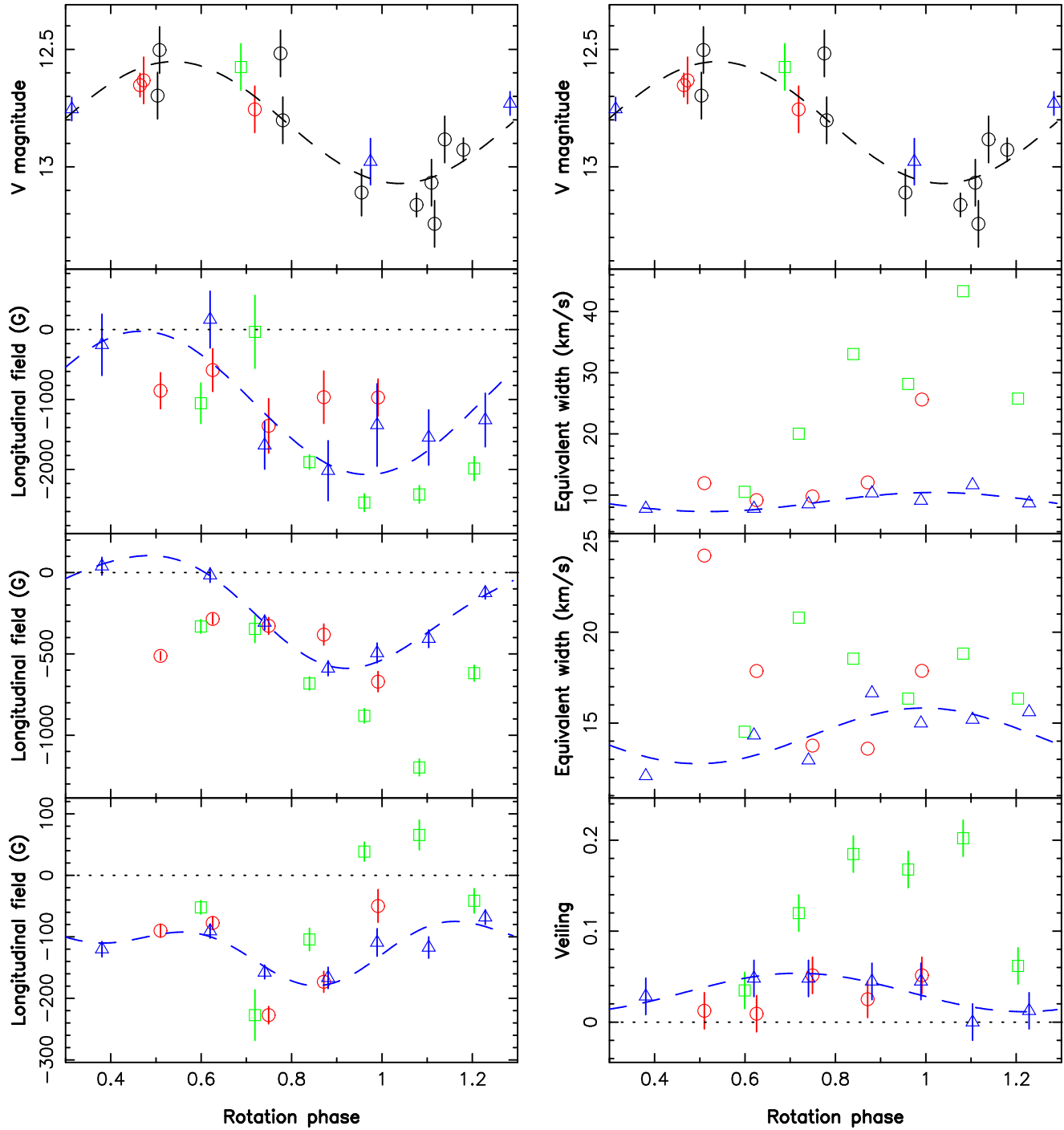


Figure 2. Temporal variations of the integrated brightness (top panels), He I D_3 (second panels), Ca II IRT (third panels) and photospheric lines (bottom panels) of AA Tau in 2008 December and 2009 January. Longitudinal field variations are shown on the left side (3 lower panels) while equivalent width and veiling variations are shown on the right side. Data collected within cycles 48.3 – 49.3, 49.3 – 50.3 and 52.3 – 53.3 are respectively plotted as red circles, green squares and blue triangles. Fits with sine/cosine waves (plus first overtones for the 2 lower left panels) are included (and shown as dashed lines) for data collected within rotation cycle 52.3 – 53.3 (to outline the amount of variability caused by rotational modulation) and for all photometric data; $\pm 1 \sigma$ error bars on data points are also shown whenever larger than symbols.

again slightly before eclipse maximum (i.e., brightness minimum, occurring at phase 1.35). The variability observed in all spectral proxies is apparently compatible with rotational modulation; the moderate phase coverage and poor phase redundancy achieved in this initial run does however not al-

low us to quantify reliably the relative strength of intrinsic variability. Emission in He I, Ca II IRT and H α lines feature equivalent widths of 14 km s^{-1} (0.027 nm), 14 km s^{-1} (0.040 nm) and 700 km s^{-1} (1.5 nm), corresponding to an average logarithmic mass-accretion rate of -9.3 ± 0.3 (in

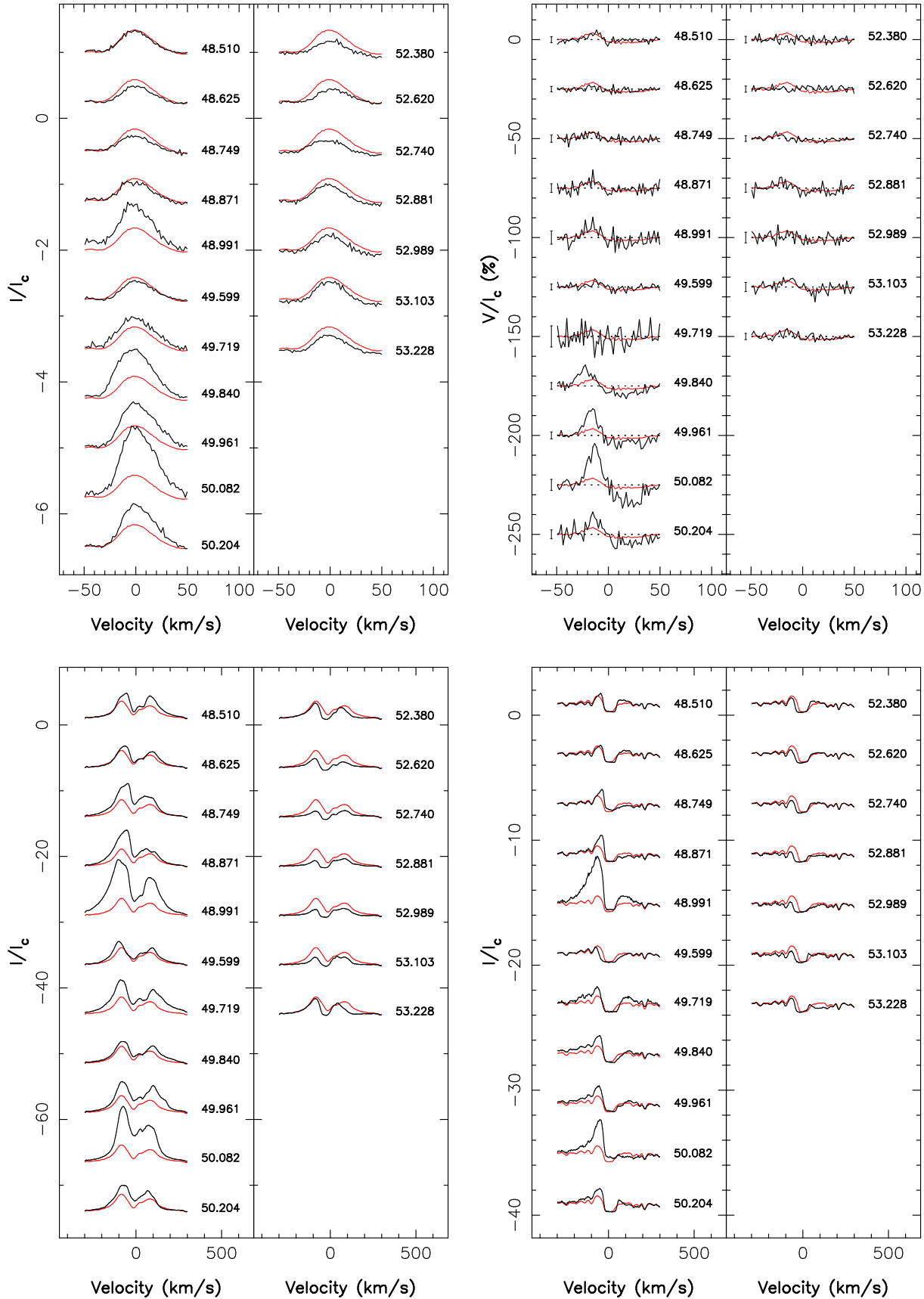


Figure 3. Variation of the He I D_3 (Stokes I : top left, Stokes V : top right), H α (bottom left) and H β (bottom right) lines of AA Tau in 2008 December (left column of each panel) and 2009 January (right column). Line fluxes in the far wings of all Stokes I profiles are close to the (unit) continuum level. To emphasize variability, the average profile over the run is shown in red. Rotation cycles (as listed in Table 1) and 3σ error bars (for Stokes V data only) are also mentioned next to each profile.

$M_{\odot} \text{ yr}^{-1}$) similar to that during the 2008/2009 run. The logarithmic surface mass-accretion rates at magnetic minimum and maximum are respectively equal to -9.6 and -9.0 , i.e., showing a larger peak-to-peak variation (but a similar level at magnetic minimum) than in 2009 January.

5 MODELLING THE SURFACE OF AA TAU

The visual inspection of all spectral proxies and their temporal variations (presented in Sec. 4) straightforwardly reveals a number of interesting results, in particular concerning the chromospheric spot at the footpoint of the accretion funnels linking AA Tau with its accretion disc. Assuming that the field within this accretion spot is mainly radial and generates the periodic longitudinal field fluctuation seen in the He I line, we can derive from the observed rotational modulation that the accretion spot is located at a latitude of about 70° (to produce a null field extremum at phase 0.5 and given that $i \simeq 70^{\circ}$, see Sec. 2) and thus that the field strength within the spot is of order of 3 kG (generating longitudinal field maxima of about 2 kG when the field reaches its minimum inclination of 50° to the line of sight). Eclipse maxima are obviously linked with (though slightly lagging) longitudinal field maxima and peak absorption in the red wing of Balmer lines, confirming that eclipses are likely due to a disc warp at the base of the accretion veil, as initially proposed by Bouvier et al. (2003) and further documented by Bouvier et al. (2007b).

Going further, and in particular quantifying how magnetic fields are distributed at the surface of AA Tau and investigating how fields connect the protostar to its accretion disc, requires a more detailed modelling of the observed profiles and their rotational modulation. This is what we propose below where we introduce a more mature and elaborate model that builds upon the preliminary version introduced in previous papers (Donati et al. 2007, 2008a). We then apply the model to our spectra of AA Tau collected in 2009 January (those from 2008 December containing too much intrinsic variability, see Sec. 4) and in 2007/2008.

5.1 Mapping magnetic field, photospheric brightness and chromospheric accretion

Our model is designed to recover simultaneously maps of the surface magnetic field, of the photospheric brightness and of the accretion-powered excess emission from sets of Stokes I and V LSD and Ca II profiles of classical T Tauri stars such as those shown in Fig. 1. We do not attempt at matching He I profiles in this paper, as the complex shape of their Zeeman signatures (see Sec. 4) would require some modelling of the velocity flows within the postshock region of accretion funnels, beyond the scope of our study. Similarly, a quantitative modelling of Balmer line profiles, requiring a full 3D description of the magnetosphere (including density and velocity fields), is postponed for future papers.

In this model, the magnetic field is described through its poloidal and toroidal components expressed as spherical-harmonics (SH) expansions (Donati et al. 2006). The spatial distribution of photospheric brightness (with respect to the quiet photosphere) and that of Ca II excess emission (with respect to the quiet chromosphere) are modelled as series

of independent pixels (typically a few thousand) on a grid covering the visible surface of the star; brightness spots are assumed to be darker than the photosphere while accretion spots are supposed to be brighter than the chromosphere. The main difference with respect to the preliminary version of the code is that the photospheric and chromospheric images are no longer assumed to be homothetic but are fitted to the data independently from one another; moreover, the quantity that we now recover for the photospheric image is brightness (rather than spottedness).

Following the principles of maximum entropy, the code automatically retrieves the simplest magnetic topology, brightness image and accretion map compatible with the series of rotationally modulated Stokes I and V LSD profiles. The reconstruction process is iterative and proceeds by comparing at each step the synthetic Stokes I and V profiles corresponding to the current images with those of the observed data set. To compute the synthetic profiles, we add up the elementary spectral contributions from each image pixel over the visible hemisphere, taking into account all relevant local parameters of the corresponding grid cell (e.g., brightness, chromospheric excess emission, magnetic field strength and orientation, radial velocity, limb angle, projected area). Since the problem is partly ill-posed, we stabilise the inversion process by using an entropy criterion (applied to the SH coefficients and to the brightness/excess emission image pixels) aimed at selecting the field topologies and images with minimum information among all those compatible with the data. The algorithm used to solve the maximum entropy problem has been adapted from that presented by Skilling & Bryan (1984) which iteratively adjusts the image by a multidirection search in the image space; in particular, this algorithm was found to be much more efficient than standard conjugate gradient techniques (see, e.g., Brown et al. 1991, for more details). The relative weights attributed to the various SH modes can be imposed, e.g., for purposely producing antisymmetric or symmetric field topologies with respect to the centre of the star (by favouring odd or even SH modes, Donati et al. 2007, 2008a).

The local synthetic photospheric Stokes I and V line profiles emerging from a given grid cell (noted I_p and V_p) are modelled using the following equations:

$$\begin{aligned} I_p &= b(\psi I_{p,m} + (1 - \psi) I_{p,q}) \\ V_p &= b\psi V_{p,m} \end{aligned} \quad (2)$$

where $I_{p,m}$ and $I_{p,q}$ are the local Stokes I photospheric profiles corresponding to the magnetic and non-magnetic areas, $V_{p,m}$ the local Stokes V photospheric profile corresponding to the magnetic areas, b ($0 < b \leq 1$) the local brightness relative to the quiet photosphere and ψ ($0 \leq \psi \leq 1$) the relative proportion of magnetic areas within the grid cell (called filling factor). For simplicity, we further assume that $I_{p,m}$ and $I_{p,q}$ differ by no more than magnetic effects, i.e., that $I_{p,q}$ equals $I_{p,m}$ taken at $\mathbf{B} = \mathbf{0}$.

Similarly, we describe the Stokes I and V Ca II emission profiles (noted I_e and V_e) with equations:

$$\begin{aligned} I_e &= I_k + eI_a = \psi(I_{k,m} + eI_{a,m}) + (1 - \psi)(I_{k,q} + eI_{a,q}) \\ V_e &= V_k + eV_a = \psi(V_{k,m} + eV_{a,m}) \end{aligned} \quad (3)$$

where I_k and V_k on the one hand, and I_a and V_a on the other hand, are the respective contributions to I and V pro-

files from the quiet chromosphere and the accretion regions, and e ($e > 0$) the local excess emission from accretion regions or equivalently the fraction of the grid cell occupied by accretion regions; the contributions from magnetic regions to I_k and I_a (respectively V_k and V_a) are denoted $I_{k,m}$ and $I_{a,m}$ (respectively $V_{k,m}$ and $V_{a,m}$) while the contributions from non-magnetic regions are denoted $I_{k,q}$ and $I_{a,q}$. For simplicity, we further assume that I_a and I_k (and similarly, $I_{a,m}$ and $I_{k,m}$, $I_{a,q}$ and $I_{k,q}$, V_a and V_k , $V_{a,m}$ and $V_{k,m}$) are homothetic, with a scaling factor denoted ϵ ($\epsilon > 1$); we also suppose that $I_{k,m}$ and $I_{k,q}$ (and thus $I_{a,m}$ and $I_{a,q}$) differ by no more than magnetic effects (just as $I_{p,m}$ and $I_{p,q}$). The filling factor ψ is finally assumed to be the same for the photospheric, chromospheric and accretion profiles, and for all grid cells. Local profiles from all grid cells are then integrated taking into account the cell visibility, projected area, limb-angle and radial velocity.

To describe the local profiles (i.e., $I_{p,m}$, $I_{p,q}$, $V_{p,m}$, $I_{k,m}$, $I_{k,q}$, $V_{k,m}$), we use Unno-Rachkovsky's equations known to provide a good description of Stokes I and V profiles (including magneto-optical effects) in the presence of both weak and strong magnetic fields (e.g., Landi degl'Innocenti & Landolfi 2004, Sec. 9.8) despite their being based on the assumption of a simple Milne-Eddington atmospheric model. For photospheric LSD profiles (i.e., $I_{p,m}$, $I_{p,q}$, $V_{p,m}$), we set the central wavelength, Doppler width and Landé factor of our equivalent line to 640 nm, 2 km s^{-1} and 1.2 respectively and adjust the average line equivalent width to the observed value (with veiling removed from all profiles); for Ca II chromospheric profiles (i.e., $I_{k,m}$, $I_{k,q}$, $V_{k,m}$), the central wavelength, Doppler width and Landé factor are set to 850 nm, 6.7 km s^{-1} and 1 respectively, the equivalent width being set to slightly below the minimum Ca II emission in our observations.

By comparing synthetic and observed profiles, we derive the spatial distributions of the local photospheric brightness b , of the Ca II excess emission e due to accretion spots, and of the magnetic vector \mathbf{B} over the stellar surface. As a side product, we also obtain estimates of several other model parameters (by selecting the image with minimum information content at a given fit accuracy), and in particular of the line rotational broadening $v \sin i$, of the RV v_{rad} , of the filling factor ψ and of the accretion profile scaling factor ϵ . Simulations demonstrate that the code can reliably reconstruct magnetic topologies, brightness images and accretion maps; in particular, it is found to be very efficient at recovering the poloidal and toroidal field components, a very useful diagnostic when studying large-scale magnetic topologies produced by dynamo processes at the surface of cool stars. Surface differential rotation patterns shearing the brightness and magnetic images can also be reliably retrieved, as demonstrated in its most recent application (Donati et al. 2010).

5.2 Application to AA Tau

The imaging model described above assumes that the observed profile variations are mainly due to rotational modulation, and possibly to surface differential rotation as well when the star is observed for at least several rotation cycles; all other sources of profile variability (and in particular intrinsic variability like flaring or short-term high-

accretion episodes) cannot be properly reproduced and thus contribute as noise into the modelling process, degrading the imaging performance and potentially even drowning all relevant information.

Filtering out significant intrinsic variability from the observed profiles of AA Tau is thus worthwhile to optimise the behaviour and convergence of the imaging code, leading us to discard our 2008 December data and to concentrate only on those collected in 2009 January and during our 2007/2008 run. For the latter 2 sets, we further need to suppress veiling, e.g., by scaling all LSD Stokes I and V photospheric profiles to ensure that unpolarized lines have the same equivalent widths; we also need to retain rotational modulation only in the variations of Ca II IRT profiles, e.g., by fitting them with a sine+cosine wave and scaling the corresponding Stokes I and V profiles to ensure that unpolarized lines match the fitted equivalent widths (see Fig. 4). While obviously no more than approximate, this procedure has the advantage of being very straightforward yet reasonably efficient, and proved successful in the case of the cTTS V2247 Oph (Donati et al. 2010). For both runs, rotational modulation in Ca II emission is found to be of order 30% peak-to-peak.

Given the moderate $v \sin i$ of AA Tau, we limit the SH expansions describing the field at $\ell = 5$. The reconstructed magnetic, brightness and accretion maps¹ of AA Tau are shown in Fig. 5 for both epochs, with corresponding fits to the data shown in Fig. 6. The overall fits are good, reproducing the data down to the noise level starting from initial reduced chi-squares of 18 and 5.5 for the 2009 January and 2007/2008 data sets respectively. Observations at both epochs (covering roughly a single rotation cycle) do not allow an estimate of surface differential rotation. Optimal fits are obtained for $v \sin i = 11.5 \pm 0.5 \text{ km s}^{-1}$ and $v_{\text{rad}} = 17.2 \pm 0.1 \text{ km s}^{-1}$, in good agreement with previous estimates (e.g., Bouvier et al. 2003, 2007b); Ca II IRT lines are found to be slightly redshifted (by about 1 km s^{-1}) with respect to photospheric lines, as usual for cTTSs (e.g., Donati et al. 2007, 2008a). We also find that filling factors of about $\psi \simeq 0.3 \pm 0.1$ provide the best fit to the far wings of the observed Stokes V profiles (see Fig. 6).

The emission profile scaling factor ϵ , describing the emission enhancement of accretion regions over the quiet chromosphere, is set to $\epsilon = 10$. This value is however somewhat arbitrary; fitting the observed strengths of emission profiles fixes $\epsilon \sum e$ rather than ϵ alone, with e describing how the excess emission from accretion regions varies over the surface of the star (see Eq 3) and $\sum e$ thus estimating the fractional area of accretion footprints. We nevertheless think that our choice of ϵ is realistic (and accurate within a typical factor of a few) given that the fractional areas of accretion footprints it yields (a few %, see below) are grossly compatible with published estimates (e.g., Valenti & Johns-Krull 2004).

The reconstructed large-scale magnetic topologies are

¹ Reconstructed maps are only shown down to latitudes of -30° ; being both strongly limb-darkened and visible for only a short amount of time, features at lower latitudes contribute little to the observed profiles and are therefore basically out of reach of imaging techniques, especially when phase coverage is moderate.

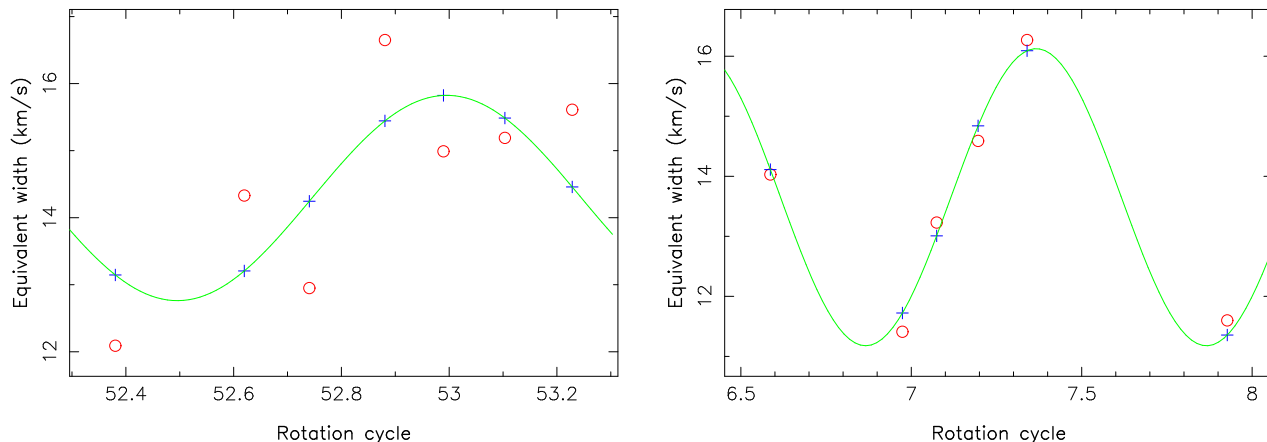


Figure 4. Measured (red open circles) and fitted (blue pluses) equivalent widths of the Ca II IRT LSD profiles throughout our 2009 January (left) and 2007/2008 (right) observing runs. The model wave (green line) providing the best (sine+cosine) fit to the data (with a period of 8.22 d) presumably traces rotational modulation, while the deviation from the fit illustrates the strength of intrinsic variability.

similar at both epochs and essentially consist in a $\simeq 2$ kG dipole inclined at about 20° to the rotation axis, concentrating about 90 – 95% of the poloidal field energy. This is about 30% weaker than predicted from the He I alone (indicating a polar field of about 3 kG, see above), likely reflecting the uncertainty in the modelling of the Ca II profiles. We thus conservatively conclude that the dipole component of AA Tau is in the range 2 – 3 kG. These estimates are grossly compatible with previous results from dipolar fits to He I spectropolarimetric data (Valenti & Johns-Krull 2004). The quadrupole/octupole components are significantly weaker, by typically a factor of 5 to 10 depending on the relative weights given to the different SH modes (see Sec. 5). We also find that the field includes a significant toroidal component in the shape of an equatorial ring of negative (i.e., clockwise) azimuthal field (0.5 – 1 kG), totalling about 15 – 20% of the magnetic energy at the surface of the star. As already mentioned in Sec. 4, this toroidal component can be straightforwardly traced back to the average shape of LSD Stokes V profiles of photospheric lines (mostly symmetric about the line centre, see Fig. 1) and can thus be considered as reliable.

The main difference between the two reconstructed magnetic images is an apparent shift of about 0.25 cycle between the phases towards which the dipoles are tilted (phase 0 in 2009 January and phase 0.25 during the 2007/2008 run). Since eclipse phases (respectively equal to 0.05 and 0.35, see Sec. 4) are also shifted by about the same amount, we can conclude that this shift essentially reflects the uncertainty on the rotation period; a slightly smaller period (of $\simeq 8.18$ d instead of 8.22 d, still compatible with the quoted uncertainty of 0.03 d of Bouvier et al. 2007b) would bring the two images (and photometric data sets) in phase with one another. Given the moderate phase coverage and the level of intrinsic variability observed on AA Tau (even in Stokes V profiles of photospheric lines, see Fig. 2), it is difficult to ascertain whether the remaining differences in the reconstructed large-scale fields at both epochs are real.

The surface brightness maps we reconstruct are also grossly similar once accounting for the phase shift between both epochs. They mostly feature a large spotted area centred at latitude $\simeq 50^\circ$, covering about 10% of the full surface

and spreading over about half the full phase range. This dark area accounts in particular for the observed Stokes I profile asymmetries (see Fig. 6 left panels) and for the corresponding RV variations. The location of this spot agrees well with the epochs of eclipse maxima, as expected from RV maxima and minima occurring respectively $\simeq 0.25$ rotation cycle before and after eclipse maxima (see Fig. 7).

Given the depth of eclipses (ranging from 0.5 to 1.5 mag), it is fairly clear that this dark region cannot fully account by itself for the observed photometric variability; color and photopolarimetric variations further demonstrate that circumstellar extinction is the main cause of the observed brightness changes (Bouvier et al. 2003; Ménard et al. 2003). Similarly, one can wonder whether the reconstructed dark region is not spurious, i.e., whether the observed line profile variations are not the direct consequence of eclipses. This is unlikely for at least two reasons. Firstly, the varying asymmetries in the observed Stokes I photospheric profiles and the corresponding RV fluctuations are known to occur at all times, even when eclipses are missing (e.g., around JD 2,451,522, Bouvier et al. 2003); our own data also demonstrate that RV variations are grossly stable and weakly affected by changes in the accretion rate and veiling strength (see Fig. 7 and bottom right panel of Fig. 2). Secondly, similar (though smaller) dark regions, more or less spatially coincident with magnetic poles, are observed on similar cTTSs (e.g., BP Tau, Donati et al. 2008a), even when not eclipsed by a warped inner disc (as AA Tau). We thus conclude that the cool region reconstructed at the surface of AA Tau is most likely real, at least its darkest parts found to grossly overlap with magnetic poles; it is however possible that some of it (e.g., the trailing extension towards phase 0.45 in the 2007/2008 image, see lower panels of Fig. 5) is spurious and caused by minor line profile changes directly caused by eclipse episodes.

The accretion maps we derive at both epochs include one high-latitude region covering about 2% of the total stellar surface (when assuming $\epsilon = 10$, see above) and shifted again by about 0.25 cycle between both runs. This accretion region is crescent-shaped, i.e., elongated along parallels and spanning a phase range of about 0.2. The brightest spot within this accretion region is leading, crossing the line-

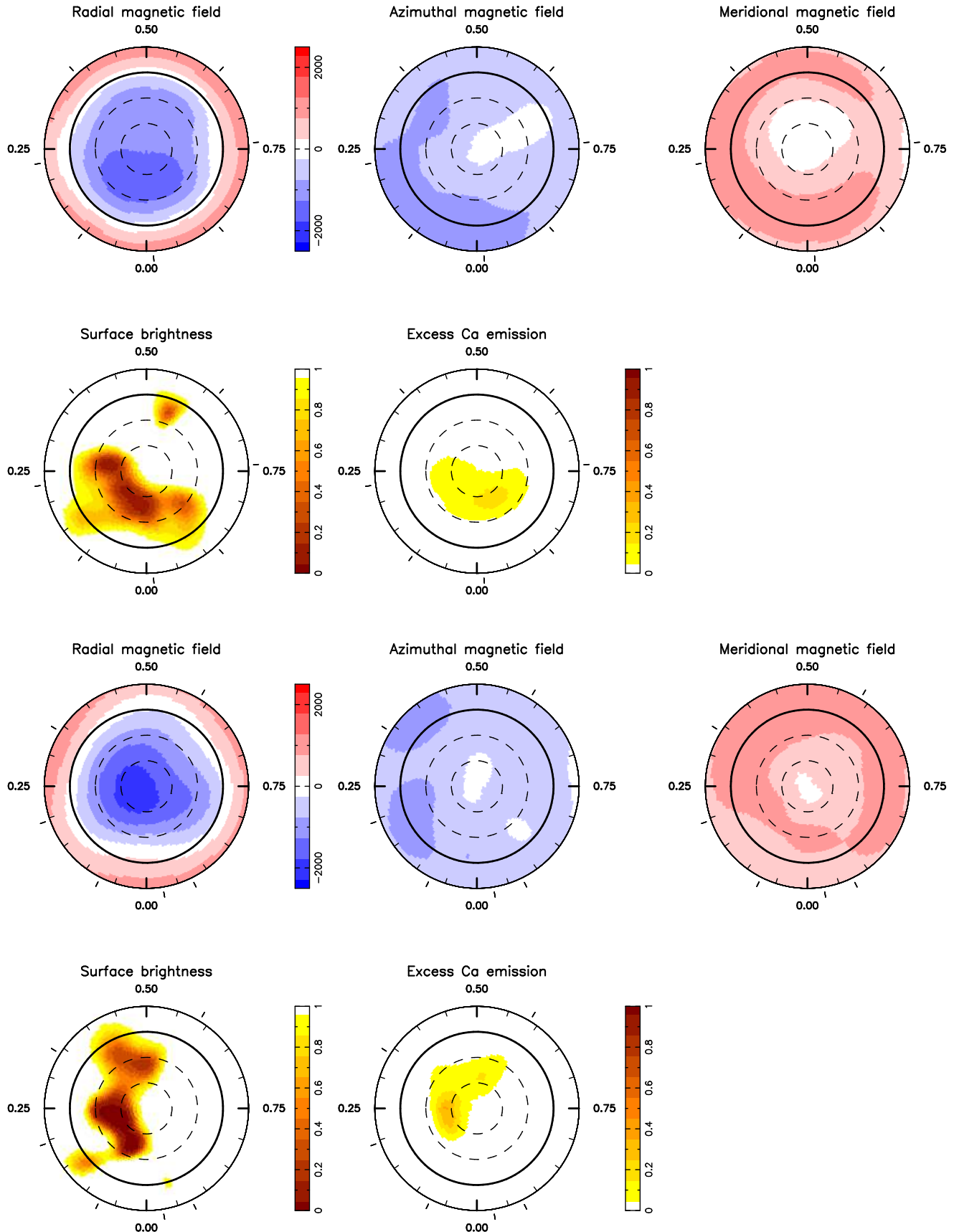


Figure 5. Maps of the radial, azimuthal and meridional components of the magnetic field \mathbf{B} (first and third rows, left to right panels respectively), photospheric brightness b and excess Ca II IRT emission e (second and fourth rows, first and second panels respectively) at the surface of AA Tau, during our 2009 January (two upper rows) and 2007/2008 (two lower rows) runs. Magnetic fluxes are labelled in G. In all panels, the star is shown in flattened polar projection down to latitudes of -30° , with the equator depicted as a bold circle

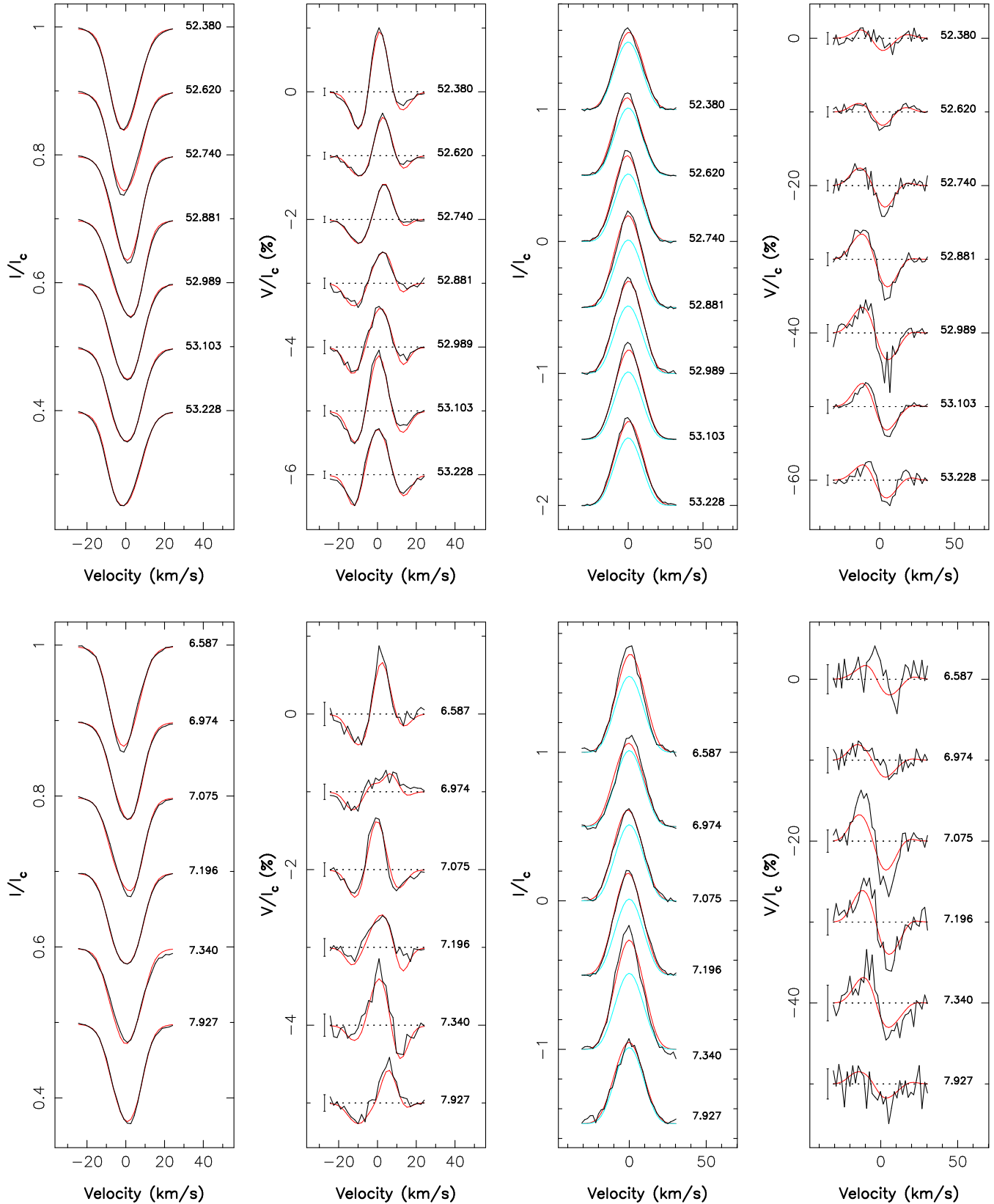


Figure 6. Maximum-entropy fit (thin red line) to the observed (thick black line) Stokes I and Stokes V LSD photospheric profiles (first two panels) and Ca II IRT profiles (last two panels) of AA Tau, for our 2009 January (upper row) and 2007/2008 (lower row) data sets. The light-blue curve in the third panels shows the (constant) contribution of the quiet chromosphere to the Stokes I Ca II profiles. Rotation cycles and 3σ error bars (for Stokes V profiles) are also shown next to each profile.

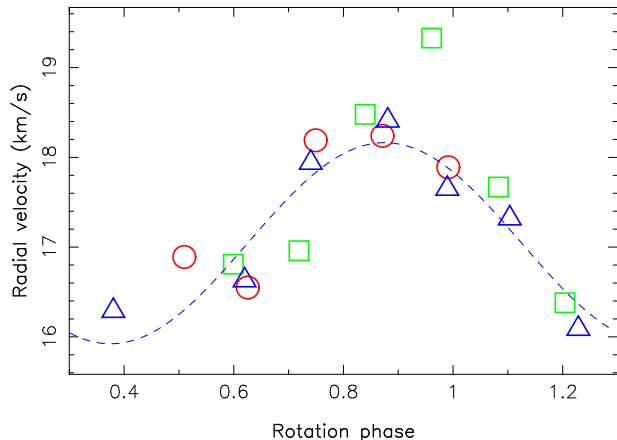


Figure 7. RV variations of photospheric lines of AA Tau in 2008 December and 2009 January. Data collected within cycles 48.3 – 49.3, 49.3 – 50.3 and 52.3 – 53.3 are respectively plotted as red circles, green squares and blue triangles, with a sine/cosine fit to the blue triangles shown (dashed line) to outline rotational modulation.

of-sight slightly before epochs of eclipse maxima (by about 0.1 cycle); it is also roughly coincident with the visible magnetic pole. These crescent-shaped accretion spots are very similar to those predicted in numerical simulation of magnetospheric accretion to slightly inclined magnetic dipoles (e.g., Romanova et al. 2004b).

6 SUMMARY AND DISCUSSION

This paper presents the first results of the MaPP project aimed at studying the impact of magnetic fields on star and planet formation. In particular, we report the detection of Zeeman signatures from the prototypical cTTS AA Tau at two different epochs (2008 December / 2009 January and 2007 December / 2008 January) and using the ESPaDOnS and NARVAL spectropolarimeters on CFHT and TBL respectively. From phase-resolved data sets, we successfully derive maps of the magnetic field, of the surface brightness and of the accretion-powered emission on AA Tau. We briefly summarize below the main results and discuss their implications for our understanding of magnetized stellar formation.

The large-scale magnetic field we reconstruct consists mostly of a 2 – 3 kG dipole slightly tilted (by about 20°) to the rotation axis, with higher SH modes of the poloidal component being at least $5\times$ smaller. This is different from BP Tau, the only other cTTS of similar mass magnetically imaged to date, where the dipole and octupole poloidal components had comparable strengths (Donati et al. 2008a). This is even more radically different from those of both lower- and higher-mass cTTSs (namely V2247 Oph and MT Ori) for which the large-scale poloidal field is much weaker and more complex (Donati et al. 2010, Skelly et al. 2010, in preparation); similar conclusions were reached for the high-mass cTTSs CV Cha and CR Cha (Hussain et al. 2009). This makes AA Tau grossly similar to mid-M dwarfs (whose large-scale fields are also found to be strong, mostly poloidal and axisymmetric, Morin et al. 2008), while higher- and lower-mass cTTSs are closer to early- and late-M dwarfs

respectively (featuring weak and complex large scale fields in average, Donati et al. 2008c; Morin et al. 2010). This strengthens the idea that magnetic fields of cTTSs are produced through dynamo processes like those of M dwarfs (Donati & Landstreet 2009). The origin of the differences between the large-scale topologies of AA Tau and BP Tau (showing very different dipole to octupole intensity ratios, > 5 and $\simeq 1$ respectively) are unclear, both stars featuring very similar masses, ages and rotation rates; we suggest that they may reflect different magnetic states in a long-term magnetic cycle.

AA Tau also includes a small but significant toroidal component totalling about 15 – 20% of the reconstructed magnetic energy, i.e., about twice as much as that of BP Tau. This is however different from mid-M dwarfs for which the toroidal component rarely exceeds a few % of the overall magnetic energy (Morin et al. 2008). We speculate that this toroidal component relates to the accretion flow, although the link between both is not clear yet; one option is that accretion is slowing down the surface of the cTTS through star/disc magnetic coupling (see below), producing a sub-surface shear, an additional interface dynamo (on top of the underlying dominant distributed dynamo operating within the bulk of the star) and the associated toroidal component. Regular magnetic monitoring of cTTSs is required to investigate this idea further.

Using the He I D_3 , Ca II IRT and H α emission fluxes (with stronger weight on the first and more reliable proxy) and the empirical correlation of Fang et al. (2009), we derive that the average logarithmic accretion rate at the surface of AA Tau (in $M_\odot \text{ yr}^{-1}$) is -9.2 ± 0.3 ; at magnetic maximum (i.e., phase 0.0), the logarithmic surface mass-accretion rate is found to vary by about an order of magnitude (from -9.4 up to -8.5) between rotation cycles, while it is roughly constant (at about -9.6) at magnetic minimum (i.e., phase 0.5). Given the estimated strength of the dipole field of AA Tau (2 – 3 kG at the pole, i.e. 1.0 – 1.5 kG at the equator, see above) and assuming an average logarithmic mass-accretion rate of -9.2 , we obtain that the radius r_{mag} at which the inner disc of AA Tau is truncated should be equal to $r_{\text{mag}} \simeq 15 R_\star$ or equivalently that $r_{\text{mag}}/r_{\text{cor}} \simeq 2$ (using the theoretical estimates of Bessolaz et al. 2008, with $B_\star \simeq 1.2 \text{ kG}$).

This result is in conflict with the conditions under which accretion can proceed, requiring $r_{\text{mag}} \leq r_{\text{cor}}$ to ensure that the effective gravity (i.e., the sum of gravitational and centrifugal forces) along accretion funnels is pointing towards the star; $r_{\text{mag}} > r_{\text{cor}}$ implies indeed that effective gravity points outwards in the inner disc regions, and thus that the magnetic star is in the propeller regime (e.g., Romanova et al. 2004a) and cannot accrete material from the disc, in contradiction with observations. In practice, the situation is likely more complex than this simplistic picture; numerical simulations of star/disc magnetic coupling in the propeller regime (and with $r_{\text{mag}} \gtrsim r_{\text{cor}}$) show for instance that a small fraction of the disc material can succeed at finding its way into the closed magnetosphere and onto the stellar surface even though most of it is expelled outwards (e.g., Romanova et al. 2005; Ustyugova et al. 2006). In this context, the mass-accretion rate at the surface of the star (i.e., the one that we estimate from emission proxies) is only

a lower limit to the mass-accretion rate in the inner disc regions.

The logarithmic accretion rate in the disc needed to enforce $r_{\text{mag}} \simeq r_{\text{cor}}$ is ranging from -8.3 to -8.0 (depending on the assumed value of B_*), i.e., 1.6 – 3.2 times larger than the maximum accretion rate observed at the surface of the star and 8 – 16 times larger than the average estimated surface accretion rate. Interestingly enough, logarithmic accretion rates at the surface of the star derived from the strongest He I emission levels typically reported in the literature (equal to about 75 km s^{-1} or 0.15 nm , e.g., Bouvier et al. 2003, 2007b) and tracing the highest-accretion phases of AA Tau, are equal to -8.2 , i.e., compatible with the mass-accretion rate in the disc that we independently derive from matching r_{mag} and r_{cor} . It confirms at least that the upper limit in the surface accretion rate that our study predicts is grossly compatible with published observations; it also suggests that AA Tau is in a state where most of the material accreting through the disc is expelled outwards (the propeller regime) and only a small amount (up to 40% in 2008 December, $\simeq 10\%$ in average, $\simeq 5\%$ in 2009 January) accreted towards the star. Our observations are in this respect qualitatively similar to results of numerical simulations of cTTSs in propeller regime (e.g., Romanova et al. 2005; Ustyugova et al. 2006).

The strong variability that mass accretion at the surface of AA Tau is subject to is another argument favouring our interpretation. It suggests in particular that the accretion variability observed for AA Tau mostly relates to the variable efficiency at which the disc material succeeds at entering the closed magnetosphere in propeller regime, rather than to an intrinsic variability of the accretion rate within the inner disc. This is also in qualitative agreement with results of numerical modelling of the propeller regime (e.g., Romanova et al. 2005) where the accretion flow from the inner disc to the surface of the star never reaches steady state and remains intrinsically variable.

The systematic lag of photometric eclipses with respect to magnetic/accretion maxima (see Sec. 4) is another independent element favouring our schematic model. Previous observations of AA Tau with the optical and UV monitors of XMM-Newton show a behaviour similar to that reported here, with UV maximum (presumably coinciding with magnetic and accretion maxima) occurring well before the optical eclipse (Grosso et al. 2007), suggesting that this is a regular phenomenon. We propose that this time delay between magnetic poles and eclipse times indicates that field lines connecting AA Tau to its inner accretion disc are twisted as a result of their different rotation rates, with leading funnel footpoints at the surface of AA Tau and a trailing accretion warp (producing the lagging variable eclipse) at $r_{\text{mag}} \gtrsim r_{\text{cor}}$.

Our study brings fresh evidence that, thanks to its strong dipole field component, AA Tau is still mainly in propeller regime, with most of the material in the inner regions of the accretion disc being expelled outwards and only a small fraction accreted towards the star. It suggests in particular that spinning down of cTTSs through star/disc magnetic coupling can potentially still be efficient at ages of about 1–2 Myr. AA Tau thus appears as an optimal laboratory for studying in more details the spinning down of cTTSs in propeller regime and for testing predictions of numerical simulations on this issue. With similarly detailed analyses

on a dozen of cTTSs, MaPP should soon bring important new material for our understanding of magnetospheric processes and their impact on the angular momentum evolution of forming Suns.

ACKNOWLEDGEMENTS

This paper is based on observations obtained at the Canada-France-Hawaii Telescope (CFHT) and at the Télescope Bernard Lyot (TBL). CFHT is operated by the National Research Council of Canada, the Institut National des Sciences de l’Univers of the Centre National de la Recherche Scientifique of France (INSU/CNRS) and the University of Hawaii; TBL is operated by INSU/CNRS.

We thank the CFHT/QSO and TBL staff for their efficiency at collecting data, as well as the referee, John Landstreet, for valuable comments that improved the paper.

The “Magnetic Protostars and Planets” (MaPP) project is supported by the funding agencies of CFHT and TBL (through the allocation of telescope time) and by CNRS/INSU in particular, as well as by the French “Agence Nationale pour la Recherche” (ANR). SGG acknowledges support by the Science and Technology Facilities Council [grant number ST/G006261/1].

REFERENCES

- Bessell M. S., Castelli F., Plez B., 1998, *A&A*, 333, 231
 Bessolaz N., Zanni C., Ferreira J., Keppens R., Bouvier J., 2008, *A&A*, 478, 155
 Bouvier J., Alencar S. H. P., Boutelier T., Dougados C., Balog Z., Grankin K., Hodgkin S. T., Ibrahimov M. A., Kun M., Magakian T. Y., Pinte C., 2007b, *A&A*, 463, 1017
 Bouvier J., Alencar S. H. P., Harries T. J., Johns-Krull C. M., Romanova M. M., 2007a, in Reipurth B., Jewitt D., Keil K., eds, *Protostars and Planets V Magnetospheric Accretion in Classical T Tauri Stars*. pp 479–494
 Bouvier J., Chelli A., Allain S., Carrasco L., Costero R., Cruz-Gonzalez I., Dougados C., Fernández M., Martín E. L., Ménard F., Mennessier C., Mujica R., Recillas E., Salas L., Schmidt G., Wichmann R., 1999, *A&A*, 349, 619
 Bouvier J., Grankin K. N., Alencar S. H. P., Dougados C., Fernández M., Basri G., Batalha C., Guenther E., Ibrahimov M. A., Magakian T. Y., Melnikov S. Y., Petrov P. P., Rud M. V., Zapatero Osorio M. R., 2003, *A&A*, 409, 169
 Brown S. F., Donati J.-F., Rees D. E., Semel M., 1991, *A&A*, 250, 463
 Cieza L. A., Schreiber M. R., Romero G. A., Mora M. D., Merin B., Swift J. J., Orellana M., Williams J. P., Harvey P. M., Evans N. J., 2010, *ApJ*, 712, 925
 Donati J., Landstreet J. D., 2009, *ARA&A*, 47, 333
 Donati J., Skelly M. B., Bouvier J., Jardine M. M., Gregory S. G., Morin J., Hussain G. A. J., Dougados C., Ménard F., Unruh Y., 2010, *MNRAS*, 402, 1426
 Donati J.-F., 2003, in Trujillo-Bueno J., Sanchez Almeida J., eds, *Astronomical Society of the Pacific Conference Series Vol. 307 of Astronomical Society of the Pacific Conference Series, ESPaDOnS: An Echelle SpectroPolarimetric Device for the Observation of Stars at CFHT*. pp 41–+

- Donati J.-F., Howarth I. D., Jardine M. M., Petit P., Catala C., Landstreet J. D., Bouret J.-C., Alecian E., Barnes J. R., Forveille T., Paletou F., Manset N., 2006, *MNRAS*, 370, 629
- Donati J.-F., Jardine M. M., Gregory S. G., Petit P., Bouvier J., Dougados C., Ménard F., Cameron A. C., Harries T. J., Jeffers S. V., Paletou F., 2007, *MNRAS*, 380, 1297
- Donati J.-F., Jardine M. M., Gregory S. G., Petit P., Paletou F., Bouvier J., Dougados C., Ménard F., Cameron A. C., Harries T. J., Hussain G. A. J., Unruh Y., Morin J., Marsden S. C., Manset N., Aurière M., Catala C., Alecian E., 2008a, *MNRAS*, 386, 1234
- Donati J.-F., Morin J., Petit P., Delfosse X., Forveille T., Aurière M., Cabanac R., Dintrans B., Fares R., Gastine T., Jardine M. M., Lignières F., Paletou F., Velez J. C. R., Théado S., 2008c, *MNRAS*, 390, 545
- Donati J.-F., Moutou C., Farès R., Bohlender D., Catala C., Deleuil M., Shkolnik E., Cameron A. C., Jardine M. M., Walker G. A. H., 2008b, *MNRAS*, 385, 1179
- Donati J.-F., Paletou F., Bouvier J., Ferreira J., 2005, *Nature*, 438, 466
- Donati J.-F., Semel M., Carter B. D., Rees D. E., Collier Cameron A., 1997, *MNRAS*, 291, 658
- Fang M., van Boekel R., Wang W., Carmona A., Sicilia-Aguilar A., Henning T., 2009, *ArXiv e-prints*
- Grankin K. N., Melnikov S. Y., Bouvier J., Herbst W., Shevchenko V. S., 2007, *A&A*, 461, 183
- Gregory S. G., Matt S. P., Donati J.-F., Jardine M., 2008, *MNRAS*, 389, 1839
- Grosso N., Bouvier J., Montmerle T., Fernández M., Grankin K., Zapatero Osorio M. R., 2007, *A&A*, 475, 607
- Hussain G. A. J., Collier Cameron A., Jardine M. M., Dunstone N., Velez J. R., Stempels H. C., Donati J.-F., Semel M., Aulancier G., Harries T., Bouvier J., Dougados C., Ferreira J., Carter B. D., Lawson W. A., 2009, *MNRAS*, pp 997–+
- Jardine M. M., Gregory S. G., Donati J.-F., 2008, *MNRAS*, 386, 688
- Johns-Krull C. M., 2007, *ApJ*, 664, 975
- Kurucz R., 1993, CDROM # 13 (ATLAS9 atmospheric models) and # 18 (ATLAS9 and SYNTHE routines, spectral line database). Smithsonian Astrophysical Observatory, Washington D.C.
- Landi degl’Innocenti E., Landolfi M., 2004, *Polarisation in spectral lines*. Dordrecht/Boston/London: Kluwer Academic Publishers
- Ménard F., Bouvier J., Dougados C., Mel’nikov S. Y., Grankin K. N., 2003, *A&A*, 409, 163
- Morin J., Donati J., Petit P., Delfosse X., Forveille T., Jardine M. M., 2010, *MNRAS*, pp 1077–+
- Morin J., Donati J.-F., Petit P., Delfosse X., Forveille T., Albert L., Aurière M., Cabanac R., Dintrans B., Fares R., Gastine T., Jardine M. M., Lignières F., Paletou F., Ramirez Velez J. C., Théado S., 2008, *MNRAS*, 390, 567
- Natta A., Testi L., Muzerolle J., Randich S., Comerón F., Persi P., 2004, *A&A*, 424, 603
- Pojmanski G., 1997, *Acta Astronomica*, 47, 467
- Romanova M. M., Ustyugova G. V., Koldoba A. V., Lovelace R. V. E., 2004a, *ApJL*, 616, L151
- Romanova M. M., Ustyugova G. V., Koldoba A. V., Lovelace R. V. E., 2004b, *ApJ*, 610, 920
- Romanova M. M., Ustyugova G. V., Koldoba A. V., Lovelace R. V. E., 2005, *ApJL*, 635, L165
- Siess L., Dufour E., Forestini M., 2000, *A&A*, 358, 593
- Skilling J., Bryan R., 1984, *MNRAS*, 211, 111
- Ustyugova G. V., Koldoba A. V., Romanova M. M., Lovelace R. V. E., 2006, *ApJ*, 646, 304
- Valenti J., Johns-Krull C., 2004, *Ap&SS*, 292, 619